(Received 14 August 2025, Accepted 22 October 2025, Scheduled 2 November 2025)

Design of Notch UWB-MIMO Antennas Based on RMS-ZINC Structure Decoupling Method

Shuming Liu, Jingchang Nan*, Yifei Wang, Licong Fan, and Jianxin Qi

College of Telecommunications, Liaoning Technical University, Huludao, TX 125000, China

ABSTRACT: Based on the current trends in wireless communication systems, a novel high-isolation dual-notch ultra-wideband (UWB) multiple-input multiple-output (MIMO) antenna is proposed, measuring 46 mm × 46 mm × 0.8 mm. The antenna is printed on an RO4350 substrate and consists of two identical antennas placed orthogonally. The antenna unit features a third-order stepped rectangular structure and employs microstrip feeding, incorporating inverted U-shaped and M-shaped grooves etched onto the antenna unit to achieve dual-notch functionality, thereby addressing electromagnetic interference issues in wireless local area networks (WLAN) operating at 5.15–5.85 GHz and 7.25–7.75 GHz. To address the issue of mutual coupling in MIMO antennas, this paper presents an innovative decoupling method known as RMS-ZINC approach. This technique involves excavating a T-shaped groove on the rear of the dielectric substrate, symmetrically aligned with the diagonal, and filling it with a dielectric material primarily composed of zinc. This material substitution effectively manipulates the coupling current paths, achieving a high isolation level of −20 dB. The experimental results show that the operating bandwidth of the antenna ranges from 2.89 to 10.19 GHz, with a peak gain of approximately 5 dB (7.15 dBi) and a maximum radiation efficiency of up to 92%. The measured results are essentially consistent with the simulated ones, indicating the practical application value of the proposed MIMO antenna with notch functionality.

1. INTRODUCTION

Wireless communication technology is a key technological innovation in the transmission and reception of information, emerging as one of the most dynamic and rapidly developing fields in communication [1]. With advancements in wireless communication technology, the demand for devices capable of high data rates and large channel capacities is increasing. MIMO antennas can fundamentally mitigate multipath effects, thereby enhancing link reliability, channel capacity, gain, bandwidth, and diversity performance [2, 3]. Progress in wireless communication technology has raised higher demands of spectrum allocation, and MIMO technology is widely used to improve spectrum efficiency. This requires that antennas function effectively in wideband communication systems and can provide high isolation [4]. UWB antennas have advantages such as abundant spectrum resources, fast transmission efficiency, strong confidentiality, and low power consumption [5]. While UWB technology meets the demands of short-distance communication [6], the relatively low radiation power of UWB antennas poses challenges for long-distance transmission. In recent years, MIMO antennas have emerged as a significant research focus due to their advantages in increasing transmission capacity and reducing multipath fading [7]. However, while designing antenna elements in a limited spatial area, electromagnetic coupling between ports can reduce the channel capacity of MIMO antennas, making inter-antenna coupling a challenging issue [8, 9]. The integration of UWB technology with MIMO technology significantly extends the transmission range of UWB systems. In practical applications, many narrowband communications, such as WiMAX (3.3–3.6 GHz) and WLAN (5.15–5.825 GHz), fall within the UWB frequency range and interfere with UWB communication systems [10]; thus, having notch characteristics in UWB antennas is essential. Consequently, UWB-MIMO antennas with notch functionalities have emerged. The implementation of notch functions primarily involves etching differently shaped grooves on the radiation unit or ground plane, or adding parasitic suppression units or resonators near the radiation unit or feed line. The techniques to achieve ultra-wideband characteristics include using radiation units with stepped or fractal structures, as well as implementing slot structures on the ground plane [11]. The performance of MIMO antennas depends on whether the received signals have low correlation. Therefore, the designed MIMO antennas must have high isolation. Common methods to enhance port isolation in MIMO antennas include using electromagnetic bandgap structures [12]; however, these structures occupy large areas and increase antenna complexity. To ensure that the isolation between antenna units in the MIMO system maintains below −15 dB across the entire operating frequency band, we propose a novel approach that achieves high isolation by replacing the dielectric material in grooves excavated on the rear side of the dielectric substrate, all while maintaining a simple and compact antenna structure [13].

2. ANTENNA DESIGNS

2.1. Antenna Unit Designs

The size of the miniaturized UWB antenna unit designed in this study is 26 mm × 18 mm. The printed circuit board is con-

* Corresponding author: Jingchang Nan (nanjingchang@lntu.edu.cn).

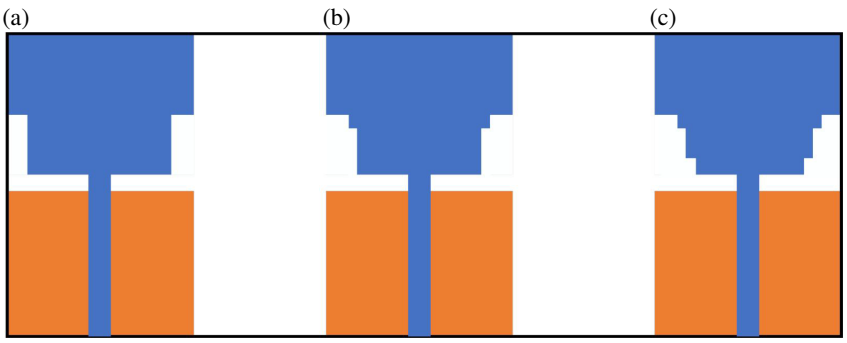

FIGURE 1. Antenna element improvement process. (a) Antenna unit l. (b) Antenna unit 2. (c) Antenna unit 3.

structed from Rogers-RO4350 material, which has a dielectric constant of 3.66 and a thickness of 0.8 mm. A 50 Ω microstrip line is used for feeding the antenna [14]. The improvement process of the antenna unit is illustrated in Figure 1. Initially, a rectangular shape is chosen for the antenna's radiating element. According to the principle of achieving UWB performance, widening the antenna's operational bandwidth can be accomplished by increasing the surface current path on the antenna. Thus, the design modification involves altering the radiating patch. By implementing a stepped cut on both sides of the radiating patch, the surface current path of the antenna is enhanced, at which point, the antenna unit functions as a simple ultra-wideband monopole antenna.

As shown in Figure 2. The design of different patch structures also influences antenna performance. When the patch is a simple rectangle, the operating bandwidth of the antenna is only 3.28 GHz. However, when a first-order stepped rectangular structure is etched into the antenna, the bandwidth increases to 3.68–8.29 GHz. With the etching of a second-order stepped rectangular structure, the bandwidth further extends to 3.57–9.65 GHz. Finally, by etching a third-order stepped rectangular structure, the bandwidth reaches an ultra-wideband range of 3.57–10.48 GHz.

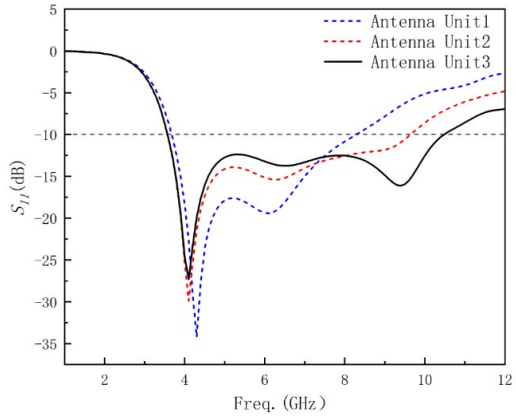

FIGURE 2. Bandwidth variation during the improvement process of the antenna element.

2.2. MIMO Antenna Design

After obtaining the aforementioned ultra-wideband monopole antenna, the antennas are arranged orthogonally to form a dual-port MIMO antenna, which enhances diversity performance and increases isolation [15]. However, the coupling between the two antenna units remains significant. To achieve higher isolation, the design incorporates a grooving method on the back of the dielectric substrate. This approach utilizes physical cutting techniques to improve the mutual coupling between the two antenna units. To generate notches for WLAN, an inverted U-shaped groove and an M-shaped groove are added to the third-order stepped rectangular radiating patch. As illustrated in Figure 3, an equivalent circuit of the dual-notch ultra-wideband antenna can be observed.

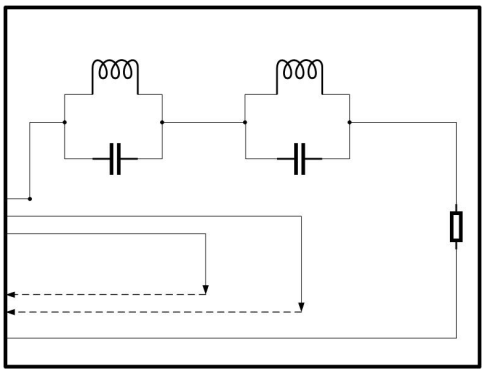

FIGURE 3. Equivalent circuit.

The length of the groove can be estimated using the following formula:

$$L = \frac{C}{2f_0\sqrt{\epsilon_{eff}}} \tag{1}$$

$$\epsilon_{eff} = \frac{\epsilon_r + 1}{2} \tag{2}$$

The formula is as follows: (L) represents the length of the groove; (c) denotes the speed of light; (f_0) is the center frequency corresponding to the stopband; (ε_r) and (ε_{eff}) are the relative permittivity and effective permittivity of the dielectric substrate, respectively. Based on Equation (1), when the center frequency is 5 GHz, the lengths of the inverted U-shaped groove and the M-shaped groove are approximately 6 mm and 4 mm, respectively. Through optimization using the electromagnetic simulation software High Frequency Structure Simulator (HFSS), the optimal stopband characteristics are achieved

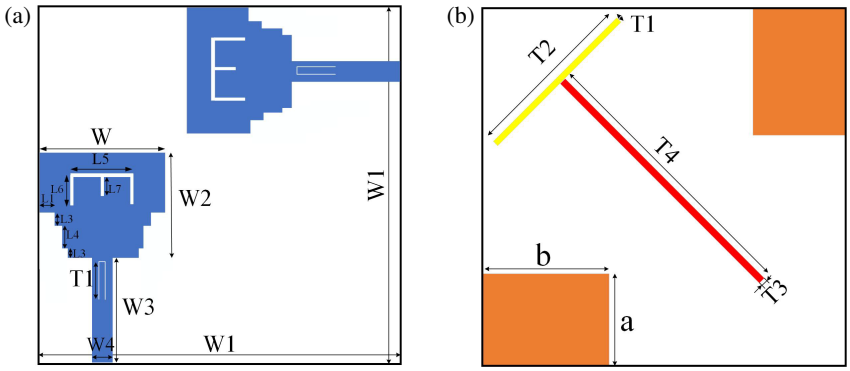

FIGURE 4. (a) Antenna front and (b) Antenna rear.

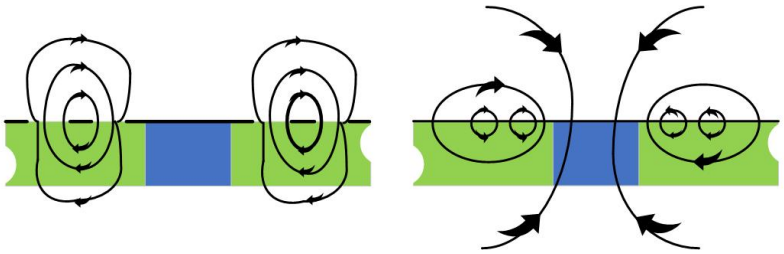

FIGURE 5. Electric field and magnetic field distribution diagram.

when the lengths of the inverted U-shaped groove and the M-shaped groove are 6.2 mm and 4 mm, respectively, which adequately cover the WLAN frequency range.

The final design of the MIMO antenna structure is shown in Figures 4(a) and (b). The antenna size parameters are shown in Table 1.

TABLE 1. The parameteric dimensions in millimeter.

Parameter	Value	Parameter	Value
a	11 mm	$L4$	3 mm
b	18 mm	$L5$	10 mm
W	18 mm	$L6$	4 mm
$W1$	46 mm	$L7$	3.2 mm
$W2$	14 mm	$L8$	37 mm
$W3$	12 mm	$T1$	6.2 mm
$W4$	2 mm	$T2$	26 mm
$L1$	2 mm	$T3$	0.8 mm
$L3$	1.5 mm	$T4$	0.4 mm

To achieve high isolation characteristics, FR-4 and zinc are placed within the grooves. FR-4 exhibits excellent mechanical and dielectric properties, along with superior thermal and moisture resistance [16]. Zinc offers good conductivity and effective electromagnetic shielding capabilities; in radio frequency interference scenarios, it acts as a reliable shielding material that can modify the distribution of the effective dielectric constant in the substrate, thereby endowing the antenna with bandgap characteristics. As shown in Figure 4, this arrangement significantly reduces mutual coupling between the two antenna units. Since the branches of the T-shaped grooves are not connected, the volumetric conductivity increases substantially when both grooves are filled with zinc, leading to an interaction in the current distribution that impairs isolation performance [17]. On the other hand, FR-4 has a relatively high dielectric performance and a relative permittivity of 4.4, which is only slightly higher than the relative permittivity of Rogers-RO4350 at 3.66. Therefore, the dielectric constant of the substrate undergoes only a minor change without significantly increasing the volumetric conductivity [18]. As the branch sections of the T-shaped groove serve as the primary decoupling structure, FR-4 is filled at the top of the T-shaped groove while zinc is used in the branch sections. This approach not only avoids affecting the current distribution in the two grooves but also offers significant decoupling effects, greatly enhancing isolation. The electric field and magnetic field distributions of the resonant structure with altered substrate materials (Replace the Media Substrate Part of The Material, RMS) are illustrated in Figure 5.

3. SIMULATION AND MEASUREMENT RESULTS ANALYSIS

3.1. Analysis of S-Parameters for MIMO Decoupling

T-shaped volumetric groove is excavated on the back of the antenna's dielectric substrate, symmetrical to the diagonal [19]. Figure 6 presents the S_{11} values of the antenna after the groove is cut. Compared to the configuration without grooves, the frequency band exhibits only minor changes and still satisfies UWB characteristics. By adjusting the length, width, and depth

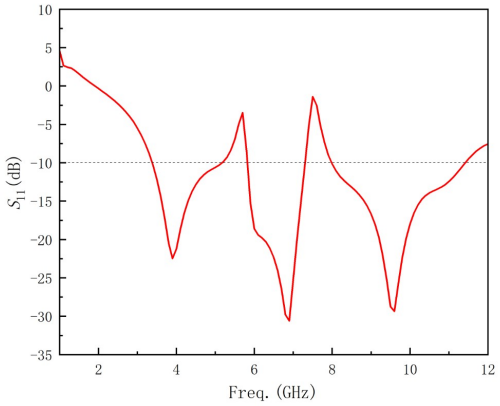

FIGURE 6. S_{11} of the antenna after slotting.

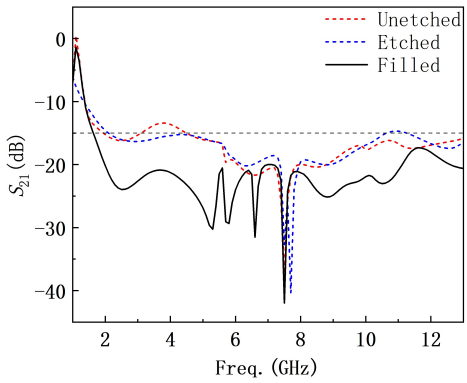

FIGURE 7. Improvement process of antenna S_{21}.

of the groove, S_{21} can be ensured to be less than -15 dB, which aligns with the properties of UWB MIMO antennas. However, as illustrated in Figure 7, the S_{21} value after grooving is slightly below -15 dB, indicating that there remains significant room for improvement in the interference resistance between the antenna units.

From a theoretical perspective, the branches filled in the T-shaped groove will generate an induced electromagnetic field in the vertical changing magnetic field, but this does not constitute a resonant system. To create resonance, it is necessary to introduce capacitance. The structure of the RMS forms a notch at the top section and the branch section of the T-shaped groove, which creates capacitance with charge accumulating on both sides. Together, the capacitance and inductance form a resonant circuit.

In the LC resonant circuit, let the inductance in the equivalent circuit be denoted as (L) and the capacitance as (C). The total inductance (L_C) in the RMS equivalent circuit and the coupling capacitance (C_c) from the notch in the branch of the T-shaped groove can be expressed by Equations (2) and (3), respectively.

$$C_c = L \cdot \frac{\epsilon}{\mu} \tag{3}$$

$$L_c = C \cdot \frac{\mu}{\epsilon} \tag{4}$$

In the equations, (L) represents the inductance of the RMS equivalent circuit; (ϵ) and (μ) denote the permittivity and permeability, respectively. The resonant frequency (f_c) of the transmission coefficient (S_{12}) can be derived from Equation (4).

$$f_c = \frac{1}{2\pi\sqrt{L_c C_c}} \tag{5}$$

Compared to other methods, the advantage of the RMS technique lies in its ability to achieve resonance at certain frequency points without requiring any structures to be added to the ground plane, thereby reducing isolation. Additionally, changes to the parameters of the RMS structure will inevitably affect the performance of the MIMO antenna units.

The designed MIMO antenna in this paper utilizes a method of replacing certain materials in the substrate. A T-shaped volumetric groove structure is excavated on the back of the dielectric substrate, symmetrical to the diagonal. Figure 7 shows the variation in (S_{21}) with and without grooves and filling materials. It can be observed that when only simple grooves are excavated in the dielectric substrate, the overall isolation performance of the antenna barely meets the requirements, with isolation slightly below -15 dB around 4.4 GHz. In contrast, after adding filling materials to the back of the antenna's dielectric substrate, the isolation performance is significantly enhanced over a bandwidth ranging from 2.78 GHz to 12.48 GHz, resulting in an overall increase of 7 dB.

The design of replacing certain materials in the substrate alters the current distribution on the surface of the ground plane, thereby reducing the mutual coupling between the two antenna ports. The purpose of this structure is to excavate the back of the dielectric substrate, interrupting the coupling current between the two antennas. This effectively extends the current path between the antenna units, which is tantamount to increasing the distance between them.

Additionally, variations in the values of $(L8)$ and $(T4)$ during the design process not only affect the antenna isolation but also influence (S_{11}). As illustrated in Figure 8, when $(L8 = T4 = 35\,\text{mm}, 36\,\text{mm}, 37\,\text{mm}, 38\,\text{mm})$, the antenna isolation is consistently below -15 dB; however, the optimal (S_{11}) performance occurs when $(L8 = T4 = 37\,\text{mm})$. This indicates that the design changes involving the replacement of certain materials in the dielectric substrate can improve isolation, and alterations in specific parameters of the structure directly affect the isolation performance. Through the continuous parameter optimization conducted with HFSS simulation software, as illustrated in Figures 9 and 10, the optimal thickness (H_2) of the substituted medium was established to be 0.5 mm.

According to the design parameters outlined in this paper, the antenna performance can also be observed through the current distribution diagrams. Figures 11(a), (b), (c), and (d) display the current distribution on the surfaces of the two antenna units when the excitation ports are set to 2 GHz, 5.8 GHz, 7.3 GHz, and 9 GHz, respectively. It is evident that the current is concentrated in the lower-left corner of the antenna, further validating the effectiveness of this decoupling structure.

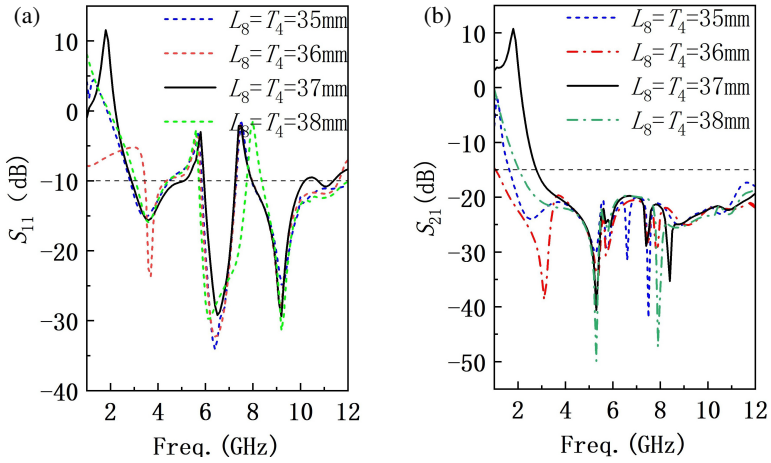

FIGURE 8. (a) S_{11} and (b) S_{21} corresponding to different values of $L8$ and $T4$.

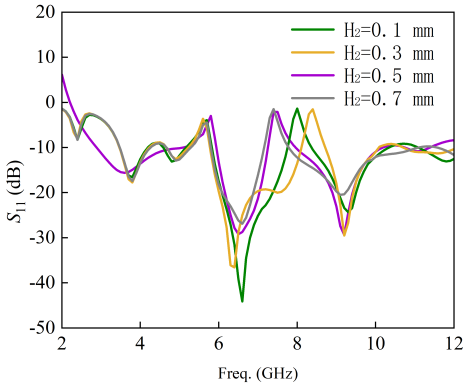

FIGURE 9. The values of S_{11} corresponding to different medium thicknesses.

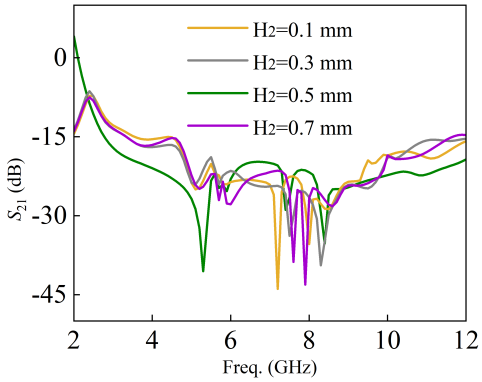

FIGURE 10. The values of S_{21} corresponding to different medium thicknesses.

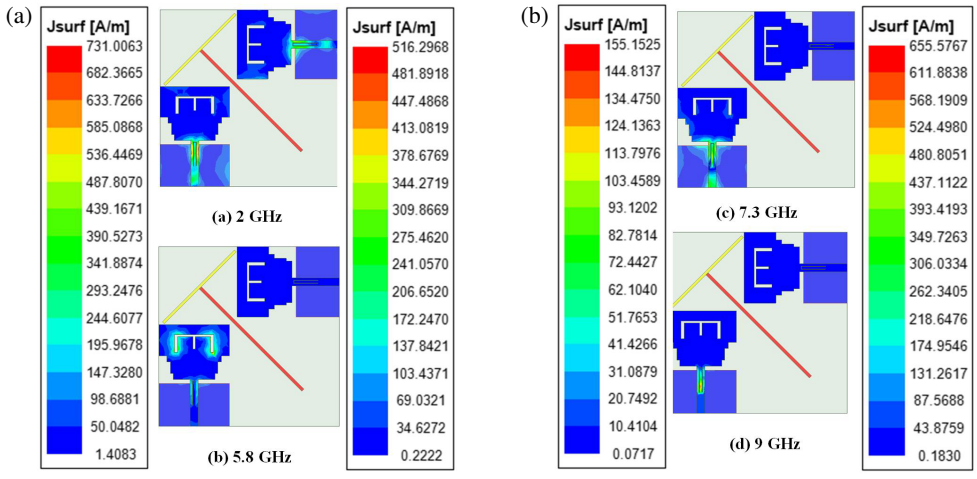

FIGURE 11. Current distribution on the surfaces of the two antenna elements.

3.2. Analysis of the *S*-Parameters for the Overall MIMO Antenna.

The physical antenna is shown in Figure 12. The S-parameter results obtained from the actual measurement of the antenna in the anechoic chamber shown in Figure 13 are displayed in Figure 14. The resonant frequency is approximately 6.5 GHz, with an (S_{11}) value of approximately -29.30 dB at this frequency, indicating that the isolation meets the requirements. The (S_{11}) and (S_{21}) curves do not completely overlap, which may be attributed to noise interference during the testing process or the

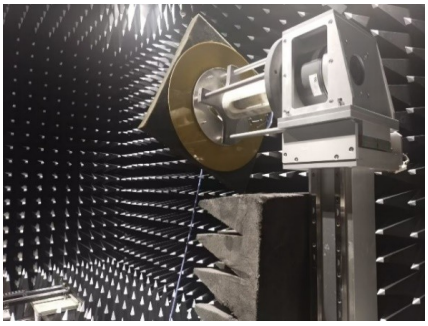

FIGURE 12. Anechoic chamber test.

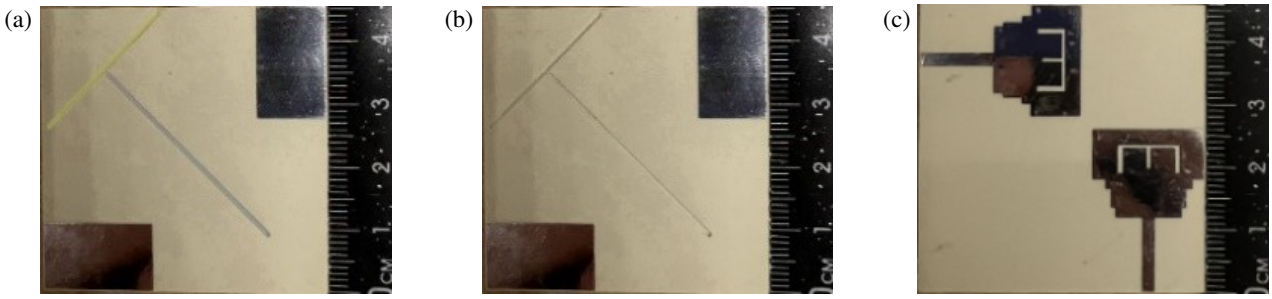

FIGURE 13. Physical diagram of the antenna.

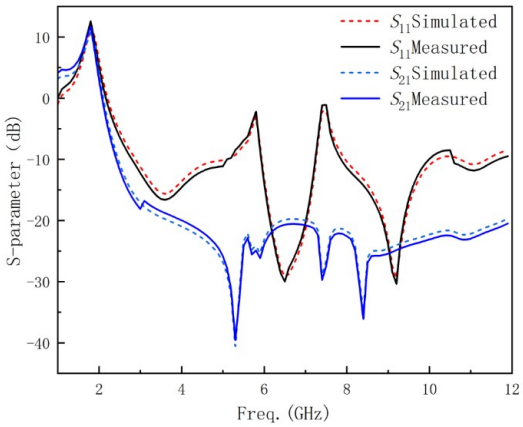

FIGURE 14. S-parameter simulation and measurement.

introduction of other materials during antenna fabrication that altered some fixed parameter values. Nevertheless, the overall simulation and measurement results are generally consistent and do not adversely affect the antenna's practical application.

3.3. Analysis of Radiation Characteristics

The antenna radiation pattern is a critical indicator of performance. Figures 15(a), (b), (c), and (d) present the measured radiation patterns of the antenna in the E-plane and H-plane at frequencies of 2 GHz, 5.8 GHz, 7.3 GHz, and 9 GHz, respectively. Since the antennas are arranged orthogonally, the radiation patterns of ports 1 and 2 are generally symmetrical along the symmetry axis. Therefore, we can focus our analysis on port 1. As shown in Figure 15, at the low-frequency end, port 1 exhibits omnidirectional characteristics in the H-plane and displays a quasi-monopole "8" shape in the E-plane. As the frequency increases, the wavelength of the antenna decreases and is no longer significantly greater than the size of the antenna. Consequently, the antenna no longer retains the characteristics of a small electric antenna, leading to changes in its radiation pattern, which will not exhibit the same radiation pattern as a monopole antenna.

Figure 16 illustrates the variation in the maximum gain and radiation efficiency of the antenna as a function of frequency. Within the operating bandwidth, the maximum gain ranges from approximately 2 dB to 8 dB. However, within the notch frequency band, the antenna's gain declines sharply to between 1.6 dB and 3.9 dB, effectively addressing electromagnetic compatibility issues between ultra-wideband and WLAN. The figure also indicates that the antenna maintains high radiation efficiency within the passband, exceeding 90%. Conversely, in the WLAN frequency band, the radiation efficiency decreases Significantly to approximately 55%.

3.4. Comparison of Antenna Performance

A comparison is made between the UWB-MIMO antennas designed in certain literature and the antenna designed in this study, with the results presented in Table 2. It is evident that most of the decoupling techniques for MIMO antennas mentioned above involve the addition of structures on the top layer or ground, which may increase design complexity or lateral dimensions. In contrast to these methods, the novel approach presented in this paper, which entails replacing material by excavating grooves on the rear of the dielectric substrate, achieves high isolation while maintaining a simple and compact antenna

TABLE 2. Comparison of MIMO antenna designs based on gain, isolation, and decoupling methods.

Literature	Gain (dBi)	Isolation Degree (dB)	Decoupling Method/Technique
[1]	3.00	15	Add branches and nodes
[6]	1.80	15	Using transparent conductive oxide patches, grounding materials, and transparent acrylic substrates
[7]	4.31	17.2	Add branches and nodes
[9]	5.60	17.0	Add branches and nodes, vertical placement
[11]	13.80	15	Change the capacitive gap
This work	7.15	20	Replace the media substrate part of the material, vertical placement

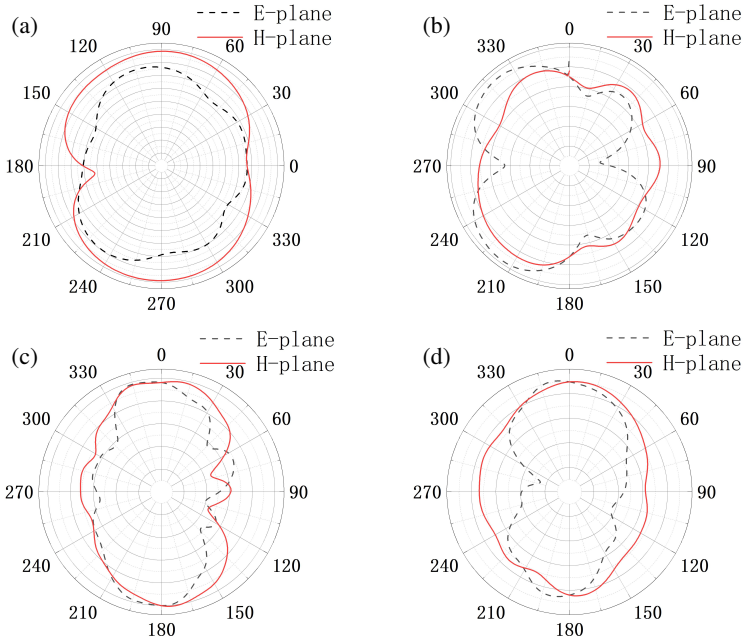

FIGURE 15. Measured radiation patterns of the E-plane and H-plane.

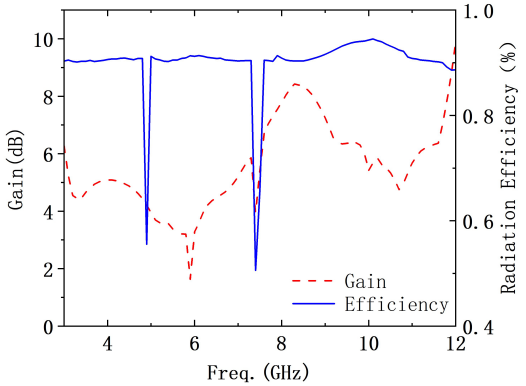

FIGURE 16. Peak gain and radiation efficiency of the antenna.

structure, and the antenna significantly outperforms most similar antennas in terms of gain, isolation, and efficiency. In the multi-port MIMO antenna discussed in reference [11], the application of the RMS-ZINC structure is shown to reduce coupling between antenna units, thereby achieving higher isolation performance. This comparison not only validates the effectiveness of the RMS-ZINC structure but also confirms that the antenna designed in this study has considerable advantages across various performance metrics.

4. CONCLUSION

This paper presents the design of a high-isolation UWB-MIMO antenna with dimensions of 46 mm × 46 mm × 0.8 mm. By etching a third-order stepped rectangular structure into the antenna's radiating patch, the current flow path is effectively enlarged, thereby extending the operational bandwidth. The primary innovation lies in the novel RMS-ZINC decoupling method, which enhances isolation by locally modifying the material properties of the substrate rather than adding circuit-level structures. This approach has proven to be highly effective, achieving isolation levels exceeding 20 dB. Furthermore, the successful integration of this technology with dual-band notch elements results in a high-gain, compact MIMO antenna, effectively mitigating interference from WLAN frequency bands.

The designed miniaturized UWB-MIMO antenna features a simple structure, efficient fabrication, and favorable performance metrics, aligning with current trends in antenna development. It has broad potential applications in wireless communication systems.

REFERENCES

[1] Desai, A., M. Palandoken, I. Elfergani, I. Akdag, C. Zebiri, J. Bastos, J. Rodriguez, and R. A. Abd-Alhameed, "Transparent 2-element 5G MIMO antenna for sub-6 GHz applications," *Electronics*, Vol. 11, No. 2, 251, 2022.

[2] Benghanem, Y., A. Mansoul, and L. Mouffok, "A compact two-element MIMO antenna with high isolation and dual band-notched characteristics for UWB communication systems," *Wireless Personal Communications*, Vol. 136, No. 2, 1107–1126, 2024.

[3] Shekhawat, S. S., D. Lodhi, and S. Singhal, "Dual band notched superwideband MIMO antenna for 5G and 6G applications," *AEU — International Journal of Electronics and Communications*, Vol. 184, 155419, Sep. 2024.

[4] Nandi, S. and A. Mohan, "A compact dual-band MIMO slot antenna for WLAN applications," *IEEE Antennas and Wireless Propagation Letters*, Vol. 16, 2457–2460, 2017.

[5] Tang, T.-C. and K.-H. Lin, "An ultrawideband MIMO antenna with dual band-notched function," *IEEE Antennas and Wireless Propagation Letters*, Vol. 13, 1076–1079, 2014.

[6] Gollamudi, N. K., Y. V. Narayana, and A. M. Prasad, "Compact and asymmetric fed modified hexagonal shaped multiple-input multiple-output (MIMO) antenna for 5G sub: 6 GHz (N77/N78 & N79) and WLAN applications," *Analog Integrated Circuits and Signal Processing*, Vol. 114, No. 1, 103–112, 2023.

[7] Tiwari, R. N., P. Singh, S. Pandey, R. Anand, D. K. Singh, and B. K. Kanaujia, "Swastika shaped slot embedded two port dual frequency band MIMO antenna for wireless applications," *Analog Integrated Circuits and Signal Processing*, Vol. 109, No. 1, 103–113, 2021.

[8] Wu, W., R. Zhi, Y. Chen, H. Li, Y. Tan, and G. Liu, "A compact multiband MIMO antenna for IEEE 802.11 a/b/g/n applications," *Progress In Electromagnetics Research Letters*, Vol. 84, 59–65, 2019.

[9] Aboelleil, H., A. A. Ibrahim, and A. A. M. Khalaf, "A compact multiple-input multiple-output antenna with high isolation for wireless applications," *Analog Integrated Circuits and Signal Processing*, Vol. 108, No. 1, 17–24, 2021.

[10] Yang, Y., Q. Chu, and C. Mao, "Multiband MIMO antenna for GSM, DCS, and LTE indoor applications," *IEEE Antennas and Wireless Propagation Letters*, Vol. 15, 1573–1576, 2016.

[11] Gopal, G. and A. Thangakalai, "Cross dipole antenna for 4G and sub-6 GHz 5G base station applications," *Applied Computational Electromagnetics Society Journal (ACES)*, Vol. 35, No. 1, 16–22, 2020.

[12] Anitha, R., P. V. Vinesh, K. C. Prakash, P. Mohanan, and K. Vasudevan, "A compact quad element slotted ground wideband antenna for MIMO applications," *IEEE Transactions on Antennas and Propagation*, Vol. 64, No. 10, 4550–4553, 2016.

[13] Desai, A., T. Upadhyaya, M. Palandoken, and C. Gocen, "Dual band transparent antenna for wireless MIMO system applications," *Microwave and Optical Technology Letters*, Vol. 61, No. 7, 1845–1856, 2019.

[14] Liu, P., D. Sun, P. Wang, and P. Gao, "Design of a dual-band MIMO antenna with high isolation for WLAN applications," *Progress In Electromagnetics Research Letters*, Vol. 74, 23–30, 2018.

[15] Zhang, S. and G. F. Pedersen, "Mutual coupling reduction for UWB MIMO antennas with a wideband neutralization line," *IEEE Antennas and Wireless Propagation Letters*, Vol. 15, 166–169, 2016.

[16] Toktas, A. and A. Akdagli, "Compact multiple-input multiple-output antenna with low correlation for ultra-wide-band applications," *IET Microwaves, Antennas & Propagation*, Vol. 9, No. 8, 822–829, 2015.

[17] Chouhan, S., D. K. Panda, M. Gupta, and S. Singhal, "Multiport MIMO antennas with mutual coupling reduction techniques for modern wireless transreceive operations: A review," *International Journal of RF and Microwave Computer-Aided Engineering*, Vol. 28, No. 2, e21189, 2018.

[18] Nadeem, I. and D.-Y. Choi, "Study on mutual coupling reduction technique for MIMO antennas," *IEEE Access*, Vol. 7, 563–586, 2018.

[19] Addepalli, T. and V. R. Anitha, "A very compact and closely spaced circular shaped UWB MIMO antenna with improved isolation," *AEU — International Journal of Electronics and Communications*, Vol. 114, 153016, 2020.